

Inter-impurity and impurity–host magnetic correlations in semiconductors with low-density transition–metal impurities

Yoshihiro Tomoda^a, Nejat Bulut^{a,b,*}, Sadamichi Maekawa^{a,b}

^a Institute for Materials Research, Tohoku University, Sendai 980-8577, Japan

^b CREST, Japan Science and Technology Agency (JST), Kawaguchi, Saitama 332-0012, Japan

ARTICLE INFO

Article history:

Received 27 September 2008

Accepted 19 November 2008

PACS:

75.50.Pp

75.30.Hx

75.40.Mg

71.55.-i

Keywords:

Dilute magnetic semiconductors

(Ga,Mn)As

Anderson model

Hirsch–Fye quantum Monte Carlo

algorithm

ABSTRACT

Experiments on (Ga,Mn)As in the low-doping insulating phase have shown evidence for the presence of an impurity band at 110 meV above the valence band. The motivation of this paper is to investigate the role of the impurity band in determining the magnetic correlations in the low-doping regime of the dilute magnetic semiconductors. For this purpose, we present results on the Haldane–Anderson model of transition–metal impurities in a semiconductor host, which were obtained by using the Hirsch–Fye quantum Monte Carlo (QMC) algorithm. In particular, we present results on the impurity–impurity and impurity–host magnetic correlations in two- and three-dimensional semiconductors with quadratic band dispersions. In addition, we use the tight-binding approximation with experimentally determined parameters to obtain the host band structure and the impurity–host hybridization for Mn impurities in GaAs. When the chemical potential is located between the top of the valence band and the impurity bound state (IBS), the impurities exhibit ferromagnetic (FM) correlations with the longest range. We show that these FM correlations are generated by the antiferromagnetic coupling of the host electronic spins to the impurity magnetic moment. Finally, we obtain an IBS energy of 100 meV, which is consistent with the experimental value of 110 meV, by combining the QMC technique with the tight-binding approach for an Mn impurity in GaAs.

© 2008 Elsevier B.V. All rights reserved.

1. Introduction

The discovery of dilute magnetic semiconductor (DMS) materials is important because of possible spintronics device applications [1–4]. The electronic state of the alloy (Ga,Mn)As, where Mn substitutes for Ga, has been investigated by various experimental methods including transport measurements, optical and photoemission spectroscopy, and scanning-tunnelling microscopy [5–10]. In the low-doping regime ($\ll 1\%$), this prototypical DMS material is insulating with clear experimental evidence for the presence of an Mn-induced impurity band located 110 meV above the valence band. For more than 2% Mn doping, the dc transport measurements indicate that the impurity band emerges with the valence band leading to a metallic state. The redshift of the mid-infrared peak observed in optical absorption in metallic samples has been attributed to inter-valence band transition instead of being due to an impurity band [8,11]. Hence, the analysis of the experimental data suggests that (Ga,Mn)As

exhibits two different regimes at low and high impurity concentrations separated by an insulator–metal transition [11].

In this paper, our purpose is to develop a microscopic understanding of the low-doping insulating phase of the DMS material (Ga,Mn)As and to shed light on the role of the impurity band in producing the magnetic correlations. For this purpose, we present numerical results on the single- and two-impurity Haldane–Anderson model of transition–metal impurities in semiconductors [12] using the Hirsch–Fye quantum Monte Carlo (QMC) method [13]. We study the influence of the electronic state of the semiconductor host on the impurity bound state (IBS) and, in turn, on the magnetic correlations which develop between the impurities and between the impurity and the host electrons. We find that, when the chemical potential μ is located between the valence band and the IBS, the ferromagnetic (FM) correlations between the impurities exhibit the longest range. We also show that the inter-impurity FM correlations are generated by the antiferromagnetic (AFM) correlations between the impurities and the host electrons. In addition, we use the tight-binding approximation to determine the host band structure and the impurity–host hybridization for the three t_{2g} orbitals of Mn in GaAs. Using tight-binding parameters consistent with photoemission measurements, we obtain an IBS energy which is in

* Corresponding author at: Institute for Materials Research, Tohoku University, Sendai 980-8577, Japan. Tel.: +81 22 215 2005; fax: +81 22 215 2006.

E-mail address: nbulut@imr.tohoku.ac.jp (N. Bulut).

agreement with the experimental value of 110 meV. Because of these results, we think that a microscopic understanding of the low-doping insulating phase of (Ga,Mn)As is possible within the Haldane–Anderson model.

The nature of the magnetic correlations in the Haldane–Anderson model of transition–metal impurities in semiconductors was studied using the Hartree–Fock (HF) approximation [14,15]. It was shown that, when the chemical potential is located between the top of the valence band and the IBS located at ω_{IBS} , long-range FM correlations develop between the impurities mediated by the AFM coupling of the valence electrons to the impurity magnetic moments. On the other hand, when the IBS becomes occupied, the spin polarization of the host split-off state cancels the polarization of the valence band, reducing the range of the FM correlations. The QMC calculations for the Haldane–Anderson model support the HF picture for the role of the IBS in producing the FM correlations [16]. The QMC results on the range of the FM correlations are in agreement with the HF predictions, however, the HF approximation underestimated the value of ω_{IBS} . These results on the magnetic correlations for $0 \lesssim \mu \lesssim \omega_{IBS}$ are different than in the metallic case, $\mu < 0$, where the inter-impurity magnetic correlations exhibit Ruderman–Kittel–Kasuya–Yosida (RKKY) oscillations with period determined by the Fermi wavevector k_f . We note that the Haldane–Anderson model was also studied within HF by Krstajić et al. [17] for DMS materials and by Yamauchi et al. [18] for hemoprotein. The role of IBS for DMS materials was also discussed by Inoue et al. [19] within HF.

In this paper, we are particularly interested in how the magnetic properties are influenced by the host electronic state, which we model using two different approaches. First, we consider the simple case where the magnetic impurity has one orbital only and the host band structure consists of quadratic valence and conduction bands. Here, in addition, we treat the impurity–host hybridization as a freely adjustable parameter. This single-orbital model is described in Section 2.1, and the QMC results for this case are presented in Sections 3 and 4 for 2D and 3D semiconductors, respectively. We study the inter-impurity and impurity–host magnetic correlations, the induced electron-density around the impurity, and show how these quantities depend on the parameters of the Haldane–Anderson model and the dimensionality of the semiconductor. These results show that the IBS and the magnetic correlations depend sensitively on the model parameters.

In order to develop a more realistic model for (Ga,Mn)As, we next use the tight-binding approximation to obtain the band structure of the bare host GaAs and the hybridization matrix elements with the three t_{2g} orbitals of Mn substituted in place of Ga. In this approach, the tight-binding parameters required for calculating the hybridization are taken from an analysis of the photoemission data on Mn 2p core level. This model is introduced in Section 2.2 and the QMC results obtained for this case are presented in Section 5. These QMC calculations keep all three of the Mn t_{2g} orbitals, and hence the multi-orbital effects are included except for those due to Coulomb repulsion between different Mn orbitals. Within this approach, we obtain an ω_{IBS} which is close to the experimental value of 110 meV. We also show that the FM correlations between the impurities weaken as the IBS becomes occupied. These results emphasize the importance of the IBS in the low-density limit of (Ga,Mn)As.

Finally, we note that the approaches taken in this paper can be extended to the case of finite concentration of Mn impurities in order to study the insulator–metal transition and the metallic state of (Ga,Mn)As observed at higher Mn concentrations.

2. Impurity model

The general model for describing transition–metal impurities in a semiconductor host is given by Haldane–Anderson Hamiltonian [12]

$$H = \sum_{\mathbf{k},\alpha,\sigma} (\epsilon_{\mathbf{k}\alpha} - \mu) c_{\mathbf{k}\alpha\sigma}^\dagger c_{\mathbf{k}\alpha\sigma} + \sum_{i,\xi,\sigma} (E_{d\xi} - \mu) d_{i\xi\sigma}^\dagger d_{i\xi\sigma} + \sum_{\mathbf{k},\alpha,i,\xi,\sigma} (V_{\mathbf{k}\alpha,i\xi} c_{\mathbf{k}\alpha\sigma}^\dagger d_{i\xi\sigma} + \text{H.c.}) + U \sum_{i,\xi} d_{i\xi\uparrow}^\dagger d_{i\xi\uparrow} d_{i\xi\downarrow}^\dagger d_{i\xi\downarrow}, \quad (1)$$

where $c_{\mathbf{k}\alpha\sigma}^\dagger$ ($c_{\mathbf{k}\alpha\sigma}$) creates (annihilates) a host electron with wavevector \mathbf{k} and spin σ in the valence or conduction bands denoted by α , and $d_{i\xi\sigma}^\dagger$ ($d_{i\xi\sigma}$) is the creation (annihilation) operator for a localized electron at impurity orbital ξ located at site i . The first term in Eq. (1) represents the kinetic energy of the host electrons, and the second term is the bare energy of the localized impurity orbitals, while the third term is due to the impurity–host hybridization. The last term represents the onsite Coulomb repulsion at the impurity orbitals. We note that here we are neglecting the Coulomb repulsion among the different impurity orbitals. The effects of the Hund couplings will be considered in a separate paper. As usual in Eq. (1), U is the onsite Coulomb repulsion, μ the chemical potential and $E_{d\xi}$ is the bare energy of the impurity orbital ξ . In addition, the hybridization matrix element is

$$V_{\mathbf{k}\alpha,j\xi} = V_{\mathbf{k}\alpha,\xi} e^{i\mathbf{k}\cdot\mathbf{R}_j}, \quad (2)$$

where \mathbf{R}_j is the coordinate of the impurity site j and $V_{\mathbf{k}\alpha,\xi}$ is the value when the impurity is located at the origin. We use the Hirsch–Fye QMC technique to study the Haldane–Anderson impurity Hamiltonian, Eq. (1), for the single- and two-impurity cases [13].

In this paper, we perform the QMC calculations using two different approaches for incorporating the host band structure and the impurity–host hybridization. In Sections 3 and 4, we consider a simple model where the impurity site contains a single-impurity orbital and the semiconductor bands have quadratic dispersion, while in Section 5 we use the tight-binding approximation for treating the three t_{2g} orbitals of Mn impurities in GaAs. In the remainder of this section, we describe these two different approaches for modelling the transition–metal impurities in semiconductors.

2.1. Single-orbital case

In Sections 3 and 4, we consider the simple case where the impurity site contains a single orbital in 2D and 3D semiconductor hosts, respectively. Hence, in this case Eq. (1) reduces to Eq. (1) of Ref. [16]. Furthermore, in these sections, we assume that the host band structure consists of one valence ($\alpha = v$) and one conduction ($\alpha = c$) bands with quadratic dispersions given by

$$\epsilon_{\mathbf{k},v} = -D(k/k_0)^2, \quad (3)$$

$$\epsilon_{\mathbf{k},c} = D(k/k_0)^2 + \Delta_C. \quad (4)$$

Here, D is the bandwidth, k_0 the maximum wavevector and Δ_C the semiconductor gap. The energy scale is determined by setting $D = 12.0$. Fig. 1 shows a sketch of the host band structure. For the Coulomb repulsion we use $U = 4.0$, and set the bare value of the impurity orbital energy to $E_d = \mu - U/2$, so that the impurity sites develop large magnetic moments. We report results for semiconductor gap $\Delta_C = 2.0$, and inverse temperature $\beta \equiv 1/T$ from 4

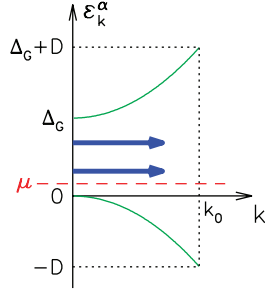


Fig. 1. (Color online) Schematic drawing of the semiconductor host bands ε_k^α (solid curves) and the impurity bound states (thick arrows) obtained with HF in the semiconductor gap. The dashed line denotes the chemical potential μ .

to 32. We also use a constant V for $V_{\mathbf{k}\alpha,\xi}$, and treat V as a free parameter.

For the single-orbital cases of Sections 3 and 4, we show QMC results on the equal-time impurity–impurity magnetic correlation function $\langle M_i^z M_j^z \rangle$ for the two-impurity Haldane–Anderson model. Here, the impurity magnetization operator is given by

$$M_i^z = d_{i\uparrow}^\dagger d_{i\uparrow} - d_{i\downarrow}^\dagger d_{i\downarrow} \quad (5)$$

and the fermion creation and annihilation operators act at a single orbital at the impurity site. In addition, we present results on the impurity–host correlation function $\langle M^z m^z(r) \rangle$ for the single-orbital and single-impurity Haldane–Anderson model. Here, the host magnetization at a distance r away from the impurity site is given by

$$m^z(r) = \sum_{\alpha=v,c} (c_{\alpha\uparrow}^\dagger(r) c_{\alpha\uparrow}(r) - c_{\alpha\downarrow}^\dagger(r) c_{\alpha\downarrow}(r)). \quad (6)$$

For the metallic case, the correlation functions $\langle M_i^z M_j^z \rangle$ and $\langle M^z m^z(r) \rangle$ were previously studied by using QMC [13,20–22]. In the single-impurity case, we also present QMC data on the square of the impurity moment, $\langle (M^z)^2 \rangle$, and the impurity susceptibility χ defined by

$$\chi = \int_0^\beta d\tau \langle M^z(\tau) M^z(0) \rangle. \quad (7)$$

The effects of IBS are clearly visible in these quantities. We also present QMC data on the charge distribution of the host material around the impurity. These QMC results are obtained using Matsubara time step $\Delta\tau = 0.25$. At $\beta = 16$, $\langle M_i^z M_j^z \rangle$ varies by a few percent as $\Delta\tau$ decreases from 0.25 to 0.125.

2.2. Tight-binding model for Mn in GaAs

In order to construct a more realistic model of (Ga,Mn)As in the dilute limit, we use the tight-binding approach to calculate $\varepsilon_{\mathbf{k}\alpha}$ and $V_{\mathbf{k}\alpha,i\xi}$ of Eq. (1) for the Mn t_{2g} orbitals. In Section 5, we will present QMC data obtained using these results on $\varepsilon_{\mathbf{k}\alpha}$ and $V_{\mathbf{k}\alpha,i\xi}$.

In this approach, the tight-binding band structure $\varepsilon_{\mathbf{k}\alpha}$ of GaAs host is obtained by keeping one s orbital and three p orbitals at each Ga and As site of GaAs with the zincblende crystal structure. We consider only the nearest-neighbor hoppings between the Ga and As sites. Fig. 2 shows the resulting band energies $\varepsilon_{\mathbf{k}\alpha}$ vs. \mathbf{k} along various directions in the face-centered-cubic (FCC) Brillouin zone for pure GaAs. The Slater–Koster parameters [23] which have been used for obtaining these results were taken from Ref. [24]. In Fig. 2, the top of the valence band is located at the Γ point, where the energy gap is 1.6 eV, which is consistent with the experimental value. This simple approximation, with nearest-neighbor hopping among the eight sp^3 orbitals, reconstructs the four

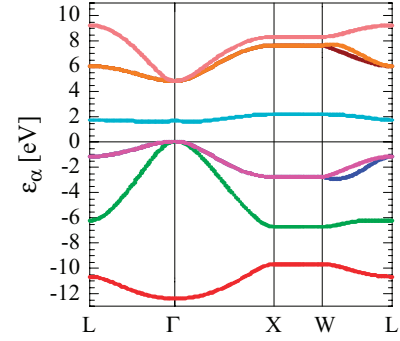


Fig. 2. (Color online) Band structure of GaAs within the tight-binding approximation.

valence bands reasonably. They are important for the impurity–host magnetic coupling in (Ga,Mn)As, because the chemical potential is located near the top of the valence band.

When an Mn impurity is substituted in place of Ga in GaAs, the five 3d orbitals of the Mn ion are split by the tetrahedral crystal field into the three-fold degenerate t_{2g} orbitals and the two-fold degenerate e_g orbitals. Since the e_g orbitals have bare energies which are much lower than the t_{2g} orbitals, we neglect the e_g orbitals and keep only the three t_{2g} orbitals of Mn in Eq. (1). In order to calculate $V_{\mathbf{k}\alpha,i\xi}$ for the Mn t_{2g} orbitals, we assume that the sp^3 orbitals of Mn are the same as those of Ga, and this way the periodic boundary conditions are also satisfied. In other words, at the Mn impurity site, we only add the three Mn t_{2g} orbitals to the GaAs host. This is a simple model for a transition–metal impurity substituted into GaAs. However, this approach allows us to take into account the effects of the host band structure beyond the quadratic dispersion. Furthermore, in Sections 3 and 4, we treat the hybridization matrix element V as a free parameter. However, here, we perform the calculations using realistic parameters for the hybridization of the 3d orbitals with the host semiconductor bands. We also note that in Ref. [25] the tight-binding and QMC techniques have been combined to study how the crystal structure of ZnO host affects the magnetic properties when Mn impurities are substituted. However, in these calculations only one of the Mn 3d orbitals is taken into account and the multi-orbital effects are not included.

Within the tight-binding approximation, the hybridization matrix element $V_{\mathbf{k}\alpha,\xi}$, Eq. (2), is obtained from

$$V_{\mathbf{k}\alpha,\xi} = \langle \psi_{\mathbf{k}\alpha} | H_0 | \varphi_\xi \rangle, \quad (8)$$

where $|\psi_{\mathbf{k}\alpha}\rangle$ is the Bloch eigenstate of the host electrons, $|\varphi_\xi\rangle$ the localized orbital eigenstate of an impurity located at the origin, and H_0 is the Hamiltonian of the system with the Coulomb repulsion turned off. In order to evaluate $V_{\mathbf{k}\alpha,\xi}$, it is necessary to determine the values of the Slater–Koster parameters between the sp^3 orbitals of GaAs and the d orbitals of Mn, which are denoted by the notation $(sp\sigma)$, $(pd\sigma)$ and $(pd\pi)$ [23]. In the following, we determine the value of $(pd\pi)$ by the general equation $(pd\pi) = (pd\sigma)/(-2.16)$ [26]. We also set $(sd\sigma) = 0$ for the following reason: when the chemical potential is near the top of the valence band, the hybridization matrix elements near the Γ point become important for the magnetic couplings. However, the s orbitals do not contribute to the three degenerate valence bands at the top of the valence band [27]. This is why we ignore the contribution of the s orbitals to hybridization and set $(sd\sigma) = 0$. The experimental estimate for the remaining Slater–Koster parameter is $(pd\sigma) = -1.1$ eV, which is obtained from the photoemission data on the Mn 2p core level with a configuration–interaction analysis based on a cluster model [28]. In Section 5, we will present QMC data obtained using $(pd\sigma) = -1.14$ eV yielding an $\omega_{IBS} = 100$ meV,

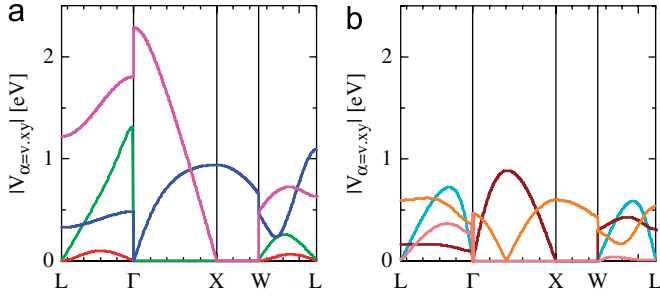


Fig. 3. (Color online) Hybridization matrix element $V_{\mathbf{k}\alpha,xy}$ of the $\xi = xy$ orbital of an Mn impurity with (a) the valence and (b) the conduction bands of GaAs vs. \mathbf{k} along various directions in the FCC Brillouin zone obtained using the tight-binding approximation.

which is in reasonable agreement with the experimental value of 110 meV for (Ga,Mn)As in the low-density limit.

Fig. 3 displays tight-binding results on $V_{\mathbf{k}\alpha,\xi}$ vs. \mathbf{k} for the $\xi = xy$ orbital, and (a) the valence and (b) conduction bands along various cuts in the FCC Brillouin zone. The values of $V_{\mathbf{k}\alpha,\xi}$ at the top of the valence and at the bottom of the conduction band are particularly important for the IBS. We note that $V_{\mathbf{k}\alpha,\xi=xy}$ takes large values near the Γ point for the top valence bands, while it is weaker for the conduction bands. In fact, the hybridization of the xy orbital with the lowest-lying conduction band vanishes at the Γ point. We also notice that $V_{\mathbf{k}\alpha,\xi}$ can be discontinuous around the high-symmetry points. In Section 5, we will present QMC data obtained using these values for $\varepsilon_{\mathbf{k}\alpha}$ and $V_{\mathbf{k}\alpha,\xi}$. In addition, for the bare energies of the impurity orbitals, we will use $E_{d\xi} = \mu - U/2$ with $U = 4.0$, so that large magnetic moments develop at the impurity sites. The QMC results do not depend sensitively on small changes in the values of $E_{d\xi}$ and U .

After obtaining $\varepsilon_{\mathbf{k}\alpha}$ and $V_{\mathbf{k}\alpha,i\xi}$ within the tight-binding model described above, we perform the QMC calculations keeping all three Mn t_{2g} orbitals. Hence, the QMC results which will be presented in Section 5 include the multi-orbital effects except for the Hund coupling. However, we will present these QMC results only for the $\xi = xy$ orbital in order to make comparisons with the single-orbital cases of Sections 3 and 4. In particular, defining the magnetization operator for $\xi = xy$ as

$$M_i^z = d_{i\xi\uparrow}^\dagger d_{i\xi\uparrow} - d_{i\xi\downarrow}^\dagger d_{i\xi\downarrow}, \quad (9)$$

we will present data on $\langle (M^z)^2 \rangle$ and the magnetic susceptibility χ , Eq. (7), for the xy orbital within the single-impurity Haldane–Anderson model. For the two-impurity case, we will present data on the inter-impurity magnetic correlation function $\langle M_1^z M_2^z \rangle$ between the xy orbitals located at the impurity sites \mathbf{R}_1 and \mathbf{R}_2 . In addition, we will discuss the magnetic correlation function between the magnetic moment of the xy orbital and the host electrons $\langle M^z m^z(\mathbf{r}) \rangle$, where the host magnetization operator at lattice site \mathbf{r} is

$$m^z(\mathbf{r}) = \sum_{\alpha} (c_{\mathbf{r}\alpha\uparrow}^\dagger c_{\mathbf{r}\alpha\uparrow} - c_{\mathbf{r}\alpha\downarrow}^\dagger c_{\mathbf{r}\alpha\downarrow}) \quad (10)$$

with α summing over the eight semiconductor bands, for the single-impurity case. In Section 5, we will see that the experimental value of ω_{IBS} is reproduced reasonably by combining the tight-binding approach with the QMC calculations. In addition, we will see that the magnetic correlations weaken as the IBS becomes occupied, in agreement with the results of Sections 3 and 4.

In the following sections, we will find that the quantitative results depend on the dimensionality and the band structure of the host material. In Sections 3 and 4, we show results for the 2D and 3D host materials with simple quadratic band dispersions.

Then, in Section 5, we discuss the case for a GaAs host using the tight binding approximation.

3. QMC results for a 2D semiconductor host

In this section, we show results for the 2D case. Here, the density of states of the pure host, ρ_0 , is a constant with a sharp cutoff at the semiconductor gap edge, which leads to stronger impurity–host coupling compared to the 3D case. Here, we present results for hybridization $\Delta \equiv \pi\rho_0 V^2$ varying from 1 to 4.

3.1. Magnetic correlations between the impurities

Figs. 4(a) and **(b)** show $\langle M_1^z M_2^z \rangle$ vs. $k_0 R$, where R is the impurity separation, for the two-impurity Anderson model for half-filled metallic ($\mu = -6.0$) and semiconductor ($\mu = 0.1$) cases. In the metallic case, $\langle M_1^z M_2^z \rangle$ exhibits RKKY-type oscillations with both FM and AFM correlations depending on the value of $k_0 R$. On the other hand, for $\mu = 0.1$, we observe FM correlations of which range increases with β .

The remainder of the data shown for the 2D case in this section are for the single-impurity Anderson model. In **Fig. 5**, we show results on $\langle (M^z)^2 \rangle$ vs. μ for various values of Δ . As T is lowered, a

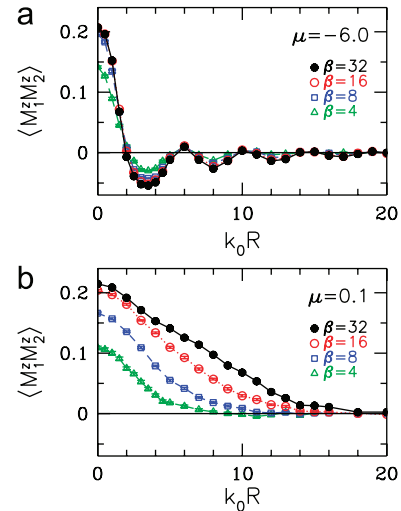


Fig. 4. (Color online) Inter-impurity magnetic correlation function $\langle M_1^z M_2^z \rangle$ vs. $k_0 R$ at various β for (a) $\mu = -6.0$ and (b) $\mu = 0.1$ for the two-impurity Haldane–Anderson model.

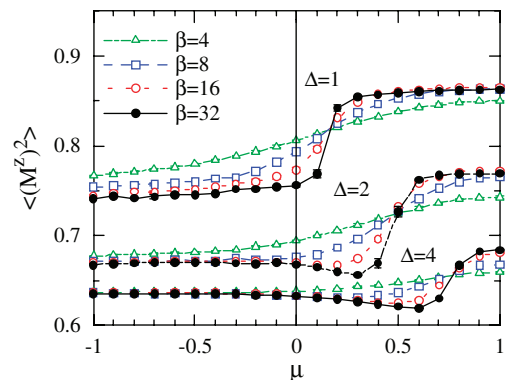


Fig. 5. (Color online) Impurity magnetic-moment square $\langle (M^z)^2 \rangle$ vs. μ at various β for $\Delta = 1, 2$ and 4 for the single-impurity Haldane–Anderson model.

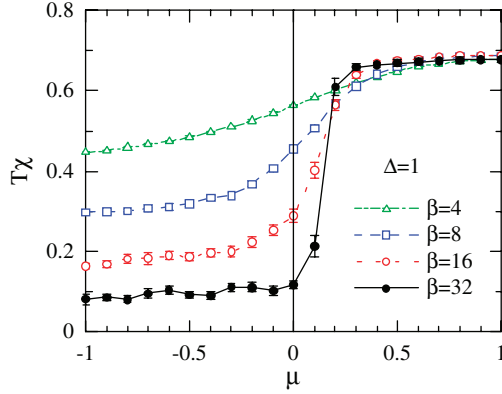


Fig. 6. (Color online) $T\chi$ vs. μ at various β for $\Delta = 1$ for the single-impurity Haldane–Anderson model.

step discontinuity develops in $\langle (M^z)^2 \rangle$ near the gap edge. The location of the discontinuity coincides with the location of IBS deduced from data on $\langle M_1^z M_2^z \rangle$, the impurity single-particle spectral weight $A(\omega)$, and the inter-impurity susceptibility χ_{12} discussed previously [16]. Hence, Fig. 5 shows that the local moment increases rapidly as the IBS becomes occupied. Here, we also observe that the moment size decreases with increasing hybridization, as expected. Fig. 6 shows $T\chi$ vs. μ for $\Delta = 1$, where we observe that a step discontinuity develops at the same location as in $\langle (M^z)^2 \rangle$ shown in Fig. 5(a). For $\mu \lesssim \omega_{\text{IBS}}$, $T\chi$ decreases with decreasing T due to the screening of the impurity moment by the valence electrons. However, for $\mu \gtrsim \omega_{\text{IBS}}$, the impurity susceptibility exhibits free-moment behavior in agreement with the role of the IBS discussed above. We note that determining the location of the IBS from $A(\omega)$ is costly in terms of computation time. For this reason, in the single-impurity case, it is more convenient to determine ω_{IBS} from data on $\langle (M^z)^2 \rangle$ vs. μ . In the remaining sections, we will use this approach for determining ω_{IBS} .

Within the HF approximation and in 2D, the range of the FM correlations is given by $(16\pi\rho_0\omega_{\text{IBS}})^{-1/2}$ for $0 < \mu < \omega_{\text{IBS}}$. This implies that the range decreases with increasing ω_{IBS} and, hence, Δ . We find that the QMC results on the maximum range of the FM correlations are in quantitative agreement with the values from the HF calculations [16]. However, we also find that the HF approximation underestimates the value of ω_{IBS} . For example, for $\Delta = 1$, HF yields $\omega_{\text{IBS}} = 0.017$, which is about an order of magnitude smaller. Hence, within HF, the long-range FM correlations are restricted to a narrow range of μ .

3.2. Impurity–host correlations

In this section, we discuss the magnetic correlations between the impurity and the host. In addition, we show results on the induced charge oscillations around the impurity site.

Figs. 7(a)–(c) show the impurity–host magnetic correlation function $s(r)$ defined by

$$s(r) = \frac{2\pi k_0 r}{n_0} \langle M^z m^z(r) \rangle \quad (11)$$

vs. $k_0 r$ for the single-impurity Anderson model for $\mu = -6.0$ (half-filled metallic), $\mu = 0.1$ (semiconductor with IBS unoccupied), and $\mu = 0.5$ (semiconductor with IBS occupied). Here, n_0 is the electron density and r is the distance from the impurity site. For $\mu = 0.1$, the coupling between the impurity and host spins is AFM for all values of $k_0 r$, while, for $\mu = -6.0$, $s(r)$ exhibits RKKY-type $2k_F$ oscillations. We also note that, for the metallic case, the magnetic correlations saturate before reaching $\beta = 32$.

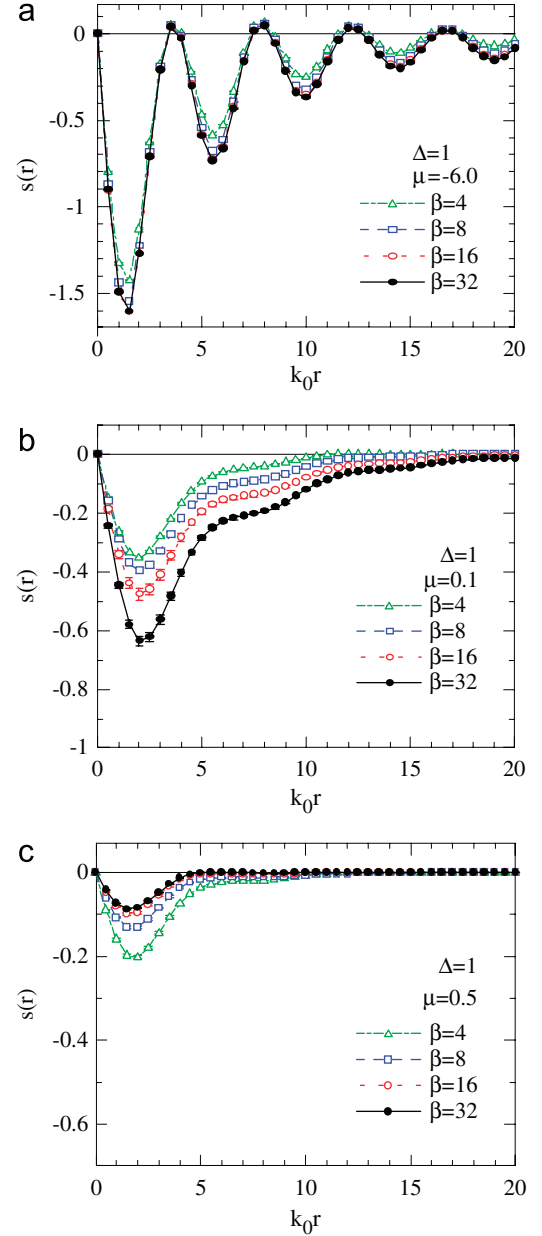


Fig. 7. (Color online) Impurity–host magnetic correlation function $s(r)$ vs. $k_0 r$ at various β for (a) $\mu = -6.0$, (b) $\mu = 0.1$, and (c) $\mu = 0.5$ for the single-impurity Haldane–Anderson model.

Comparison of Figs. 7(b) and 4(b) for $\mu = 0.1$ shows that the AFM impurity–host coupling produces the FM correlations between the impurities.

As seen in Fig. 7(c), when μ is increased to 0.5, the AFM correlations between the impurity and host spins become much weaker. This is because the IBS becomes occupied for $\mu > 0.1$. Within the HF approximation [14,15], the FM interaction between the impurities is mediated by the impurity-induced polarization of the valence electron spins, which exhibit an AFM coupling to the impurity moments. The impurity–host hybridization also induces host split-off states at the same energy as the IBS. When the split-off state becomes occupied, the spin polarizations of the valence band and the split-off state cancel. This causes the long-range FM correlations between the impurities to vanish. These QMC and HF results emphasize the role of the IBS in determining the range of the magnetic correlations for a semiconductor host.

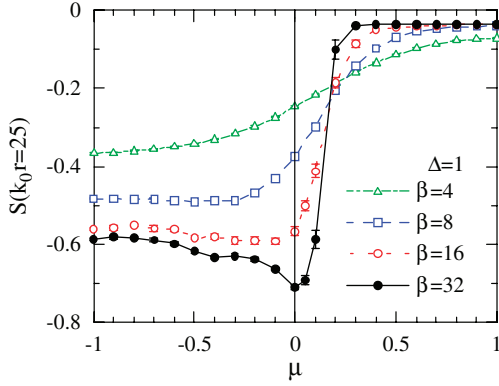


Fig. 8. (Color online) $S(k_0 r = 25)$ vs. μ at various β for the single-impurity Haldane–Anderson model.

The total magnetic coupling of the impurity magnetic moment to the host is obtained from

$$S(k_0 r) = \int_0^{k_0 r} d(k_0 r') S(r'). \quad (12)$$

Fig. 8 shows $S(k_0 r = 25)$ vs. μ for $\Delta = 1$ at various β . Here, we see that the impurity becomes magnetically decoupled from the host when $\mu \gtrsim \omega_{IBS}$.

Next, in Fig. 9, we show the modulation of the charge density around the impurity. Here, we plot $p(r)$ vs. $k_0 r$, where $p(r)$ is defined by

$$p(r) = \sum_{\alpha=v,c} \frac{2\pi k_0 r}{n_0} (n_{\alpha}(r) - n_{\alpha}(\infty)) \quad (13)$$

with $n_{\alpha}(r) = \sum_{\sigma} \langle c_{\alpha\sigma}^{\dagger}(r) c_{\alpha\sigma}(r) \rangle$. For the metallic case of $\mu = -6.0$, we observe long-range RKKY-type of oscillations in $p(r)$. When $\mu = 0.1$, the charge density around the impurity is depleted up to $k_0 r \approx 20$ at these temperatures. This depletion represents the extended valence hole which forms around the impurity. However, for $\mu = 0.5$, the induced charge density decreases significantly as T is lowered, because now the IBS is occupied. We next integrate $p(r)$,

$$P(k_0 r) = \int_0^{k_0 r} d(k_0 r') p(r') \quad (14)$$

and plot $P(k_0 r = 25)$ vs. μ in Fig. 10. We observe that the total charge density around the impurity is most depleted when $0 \lesssim \mu \lesssim \omega_{IBS}$, which is due to the valence hole induced around the impurity. In the metallic case, the induced charge density is oscillatory and has a long range as we have seen in Fig. 9(a). As μ approaches the gap edge, the electron density around the impurity is depleted. However, when $\mu \gtrsim \omega_{IBS}$, we see that this depletion is cancelled by the extended charge density of the split-off state.

4. QMC results for a 3D semiconductor host

In this section, we discuss the 3D case, where the hybridization parameter $\pi V^2 N(0)$ vanishes at the gap edge because of the vanishing of $N(0)$ of the pure host. Hence, the impurity–host coupling near the gap edge is much weaker compared to the 2D case. Consequently, the FM correlations between the impurities have a shorter range. We find that the dimensionality of the host material strongly influences the magnetic correlations. In particular, we see that the IBS does not exist in 3D unless the hybridization is sufficiently large.

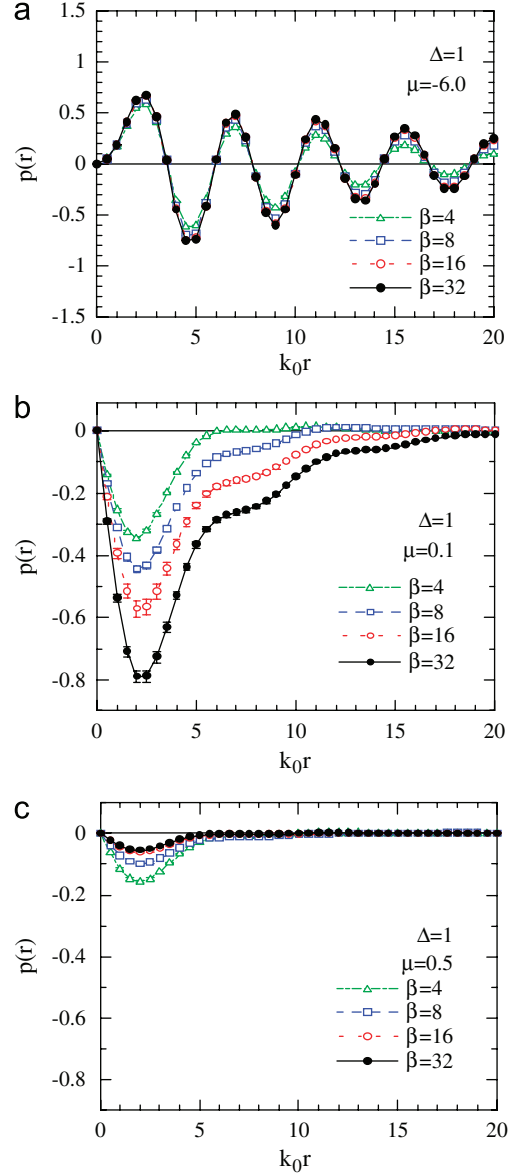


Fig. 9. (Color online) $p(r)$ vs. $k_0 r$ for $\Delta = 1$ and (a) $\mu = -6.0$, (b) 0.1 and (c) 0.5 for the single-impurity Haldane–Anderson model.

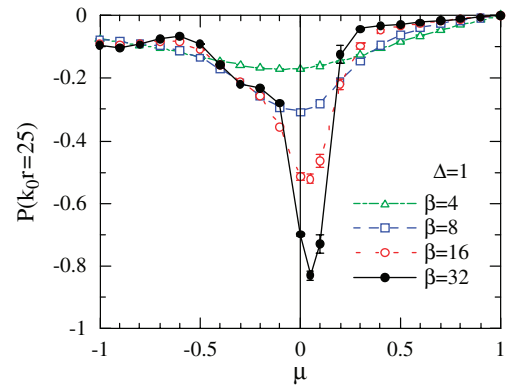


Fig. 10. (Color online) $P(k_0 r = 25)$ vs. μ at various β for the single-impurity Haldane–Anderson model.

Here, we define hybridization as $\Delta = \pi \rho_0^* V^2$ where ρ_0^* is the density of states when the valence band is half-filled, $\rho_0^* = k_0^3 / (4\sqrt{2}\pi^2 D)$. This choice allows us to use comparable

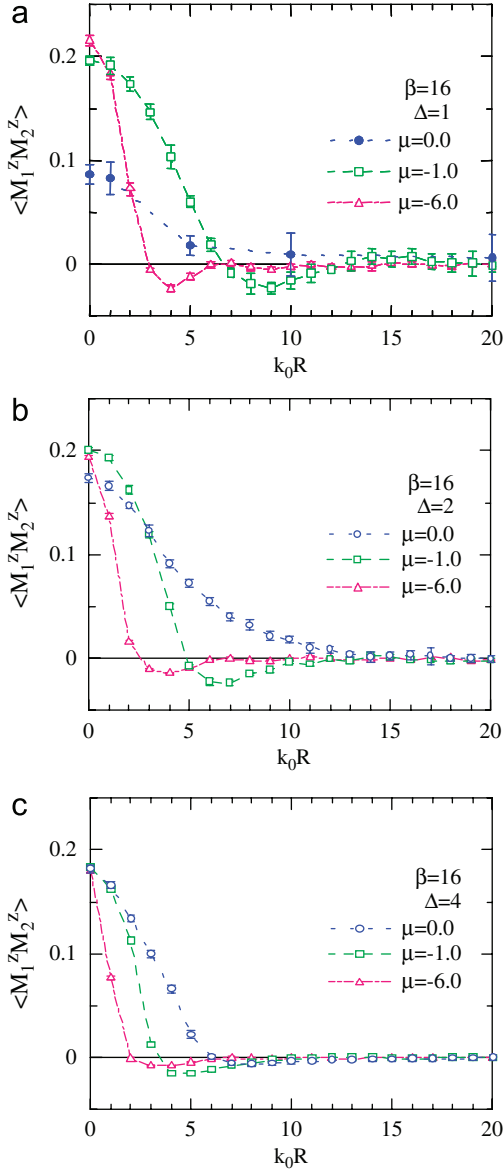


Fig. 11. (Color online) $\langle M_1^z M_2^z \rangle$ vs. $k_0 R$ at $\beta = 16$ and various μ for hybridization (a) $\Delta = 1.0$, (b) 2.0 and (c) 4.0 for the two-impurity Haldane-Anderson model in the 3D case.

values for the hybridization matrix element V when we compare the 2D and 3D results. In the following, we present results for $\Delta = 1, 2$ and 4.

Figs. 11(a)–(c) show $\langle M_1^z M_2^z \rangle$ vs. $k_0 R$ at various values of μ for $\Delta = 1, 2$ and 4. These results are for $\mu = -6.0, -1.0$ and 0.0. We observe that, for $\Delta = 1$, the FM correlations between the impurities weaken as μ approaches the top of the valence band. On the other hand, for $\Delta = 2$ and 4, the FM correlations are stronger for $\mu = 0.0$. This is because, for $\Delta = 1$, the IBS does not exist in a 3D host, as we will see later in Fig. 13, which shows results on $\langle (M^z)^2 \rangle$ vs. μ .

Fig. 12 shows the impurity–host magnetic correlation function $s(r)$ vs. $k_0 r$ for the single-impurity case. In 3D, $s(r)$ is defined by

$$s(r) = \frac{4\pi(k_0 r)^2}{n_0} \langle M^z m^z(r) \rangle. \quad (15)$$

We see that the impurity–host coupling weakens rapidly for $\mu \geq 0.0$. These figures show that, in 3D and for $\Delta = 2$, the IBS is located at $\omega_{IBS} \approx 0.0$, which is consistent with the results on

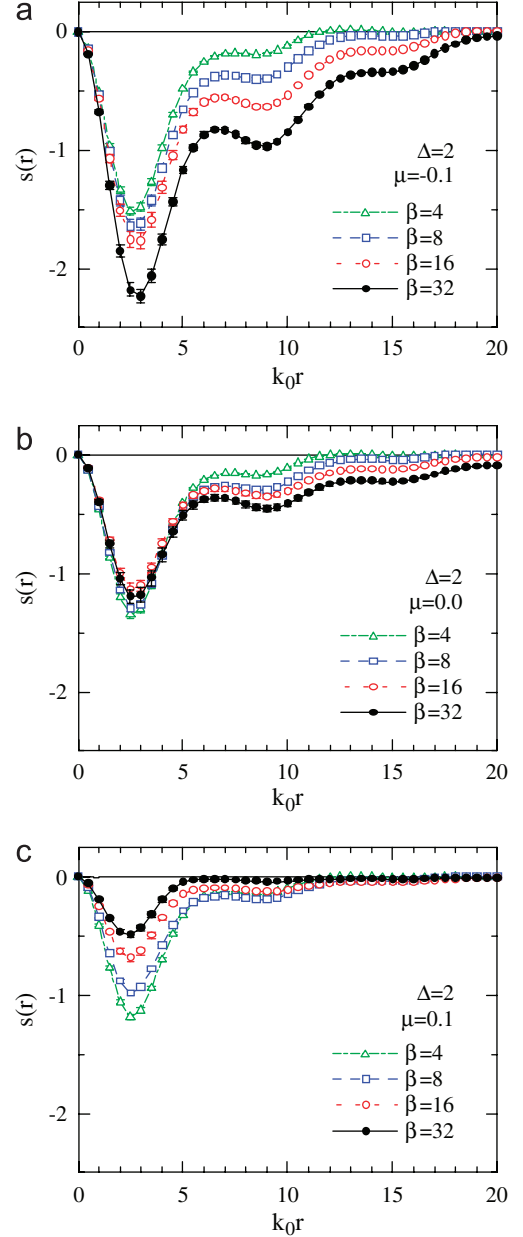


Fig. 12. (Color online) $s(r)$ vs. $k_0 r$ at various β for $\Delta = 2$ and for (a) $\mu = -0.1$, (b) 0.0 and (c) 0.1 for the single-impurity Haldane-Anderson model in a 3D host.

$\langle (M^z)^2 \rangle$ shown in Fig. 13. In Fig. 13, for $\Delta = 1$, we do not observe the development of a discontinuity for temperatures down to $\beta = 32$. For $\Delta = 2$, we observe the development of a step centered at $\mu \approx 0.0$, as β increases. For $\Delta = 4$, a step discontinuity at $\mu \approx 0.3$ is clearly observed. So, in 3D the IBS exists only for sufficiently large values of the hybridization matrix element V . This is consistent with the dependence of the IBS on the dimensionality in the $U = 0$ case. These results show that the dimensionality of the host material strongly influences the magnetic properties.

The results presented in Sections 3 and 4 show that the density of states of the pure host at the gap edge and the value of the hybridization matrix element are crucial in determining presence and the location of the IBS. The IBS is in turn important in determining the magnetic properties of the systems when transition metal impurities are substituted into a semiconductor host. This means that the electronic state of the pure host material will also be crucial in determining the magnetic properties. In the

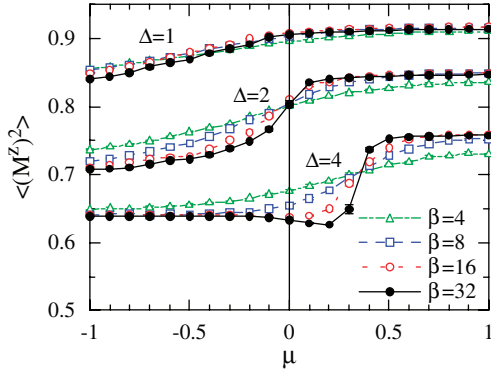


Fig. 13. (Color online) Impurity magnetic-moment square $\langle (M_z^z)^2 \rangle$ vs. μ at various β for (a) $\Delta = 1, 2$ and 4 for the single-impurity Haldane–Anderson model in a 3D host.

next section, we explore the consequences of a more realistic band structure for a GaAs host using the tight-binding approximation.

5. QMC results for the tight-binding model of an Mn impurity in GaAs

In this section, we present QMC data obtained within the tight-binding model of an Mn impurity in GaAs, which was introduced in Section 2.2. Here, we have performed the QMC calculations keeping all three of the Mn t_{2g} orbitals in Eq. (1), hence this approach includes the multi-orbital effects except for the Hund coupling. In addition, we use a more realistic description of the semiconductor bands $\varepsilon_{\mathbf{k}\alpha}$ for GaAs compared to that of Sections 3 and 4. Furthermore, the hybridization $V_{\mathbf{k}\alpha,\xi}$ is determined by the tight-binding approach using parameters consistent with photoemission measurements on Mn in GaAs, instead of being a free parameter. The following QMC results are obtained for the Slater–Koster parameters $(pd\sigma) = -1.14$ eV, $(sd\sigma) = 0$ eV, and $(pd\pi) = (pd\sigma)/(-2.16)$.

Fig. 14 shows $\langle (M_z^z)^2 \rangle$ and $T\chi$ vs. μ for the xy orbital near the top of the valence band for the single-impurity Haldane–Anderson model. Here, the development of a step discontinuity in the semiconductor gap is clearly seen as T decreases down to 180 K. At low T and for $(pd\sigma) = -1.14$ eV, the inflection point of the discontinuity occurs at 100 meV, which implies that $\omega_{IBS} = 100$ meV. This is in good agreement with the experimental value of 110 meV, especially if we note that the estimate of $(pd\sigma)$ from the photoemission experiments is -1.1 eV.

In order to understand how sensitively ω_{IBS} depends on the Slater–Koster parameters, we repeated these calculations for different values of $(pd\sigma)$ keeping $(sd\sigma) = 0$ and $(pd\pi) = (pd\sigma)/(-2.16)$. For $(pd\sigma) = -1.4$ eV, we found $\omega_{IBS} \approx 300$ meV, while for $(pd\sigma) = -1.0$ we obtained a more smeared discontinuity in $\langle (M_z^z)^2 \rangle$ vs. μ centered at $\mu \approx 0$.

Next in Fig. 15, we display $\langle M_1^z M_2^z \rangle$ vs. the impurity separation in lattice units, $|\mathbf{R}|/a$, for the xy orbital in the case of two Mn impurities substituted into Ga sites. Since we keep three orbitals at each Mn site, these calculations are more costly in terms of computer time. In this case, we present data for $T = 1500$ and 730 K. The Hirsch–Fye algorithm for the single- and two-impurity Anderson model does not have the fermion sign problem. Hence, by using sufficient amount of computer time it is possible, in principle, to extend the calculation of $\langle M_1^z M_2^z \rangle$ to lower temperatures. Even though the data on $\langle M_1^z M_2^z \rangle$ are at high temperatures, the effect of the IBS is observable. For $T = 730$ K and $\mu = 0.0$, the FM correlations extend up to 1.5a, however the FM correlations weaken as μ approaches ω_{IBS} . We note that the spatial extent of

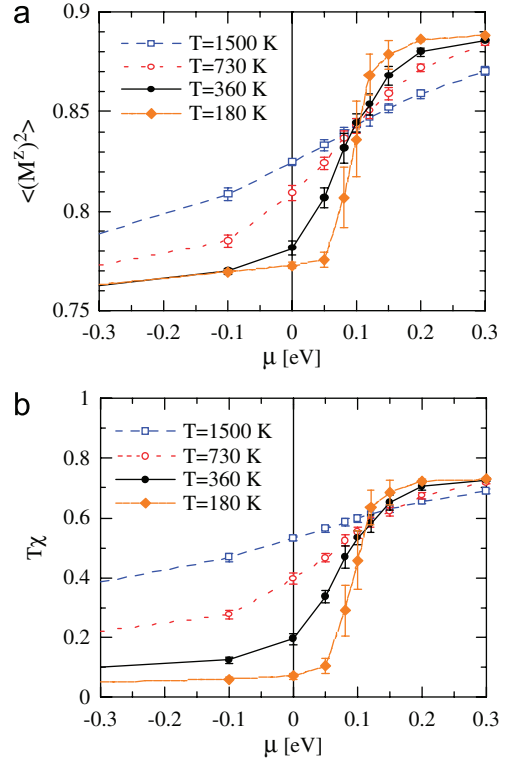


Fig. 14. (Color online) (a) $\langle (M_z^z)^2 \rangle$ and (b) $T\chi$ vs. μ for an Mn xy orbital obtained using the tight-binding model. Here, the top of the valence band is located at $\mu = 0$.

the Mn–Mn interaction in low-density (Ga,Mn)As was also considered by using the tight-binding approximation and perturbative techniques in Ref. [29].

Finally, we discuss the correlations between the host electronic spins and the magnetic moment of the xy orbital at the Mn site for the single-impurity case. In Fig. 16, we plot $\langle M^z m^z(\mathbf{r}) \rangle$ vs. the impurity distance $|\mathbf{r}|/a$ for various values of μ and T . Here, we denote the first-neighbor As site by As^1 , the second-neighbor Ga site by Ga^2 , and so on. These results show that the development of the AFM correlations between the magnetic moment of the xy orbital and the neighboring host electrons as T is lowered down to 360 K. We also observe the weakening of the AFM correlations as μ approaches ω_{IBS} .

Using the tight-binding results for $\varepsilon_{\mathbf{k}\alpha}$ and $V_{\mathbf{k}\alpha,\xi}$ as input, in this section, we have performed the QMC simulations to study the magnetic properties (Ga,Mn)As in the low-density limit. These results are similar to those presented in Sections 3 and 4 for the single-orbital case with simple band structure. In particular, we saw that, by using a realistic model for the host band structure and host-impurity hybridization of (Ga,Mn)As, it is possible to obtain an accurate value for ω_{IBS} . Such quantitative agreement supports the physical picture described in this paper for the origin of the FM correlations in DMS in the low-density limit.

6. Discussion

The computational approaches taken in this paper can be extended to study the case of finite density of Mn impurities in GaAs. Here, we have reported results for the single- and two-impurity cases. However, the Haldane–Anderson model can be studied for a finite density of impurities using the Hirsch–Fye QMC algorithm. This type of investigation could shed light on the

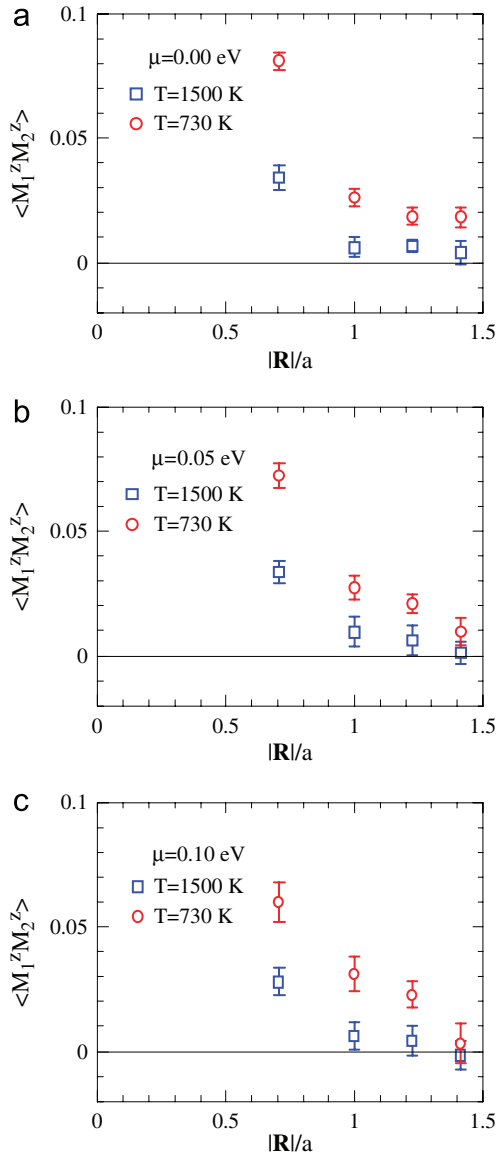


Fig. 15. (Color online) Inter-impurity magnetic correlation function ($\langle M_i^z M_j^z \rangle$) vs. R/a at various T for (a) $\mu = 0.00$ eV, (b) 0.05 eV and (c) 0.10 eV for the two-impurity Haldane–Anderson model within the tight-binding model. Here, M_i^z is the magnetization operator at the Mn xy orbital.

metal–insulator transition encountered in the DMS materials at finite density of impurities. In addition, it could help to understand the nature of the metallic state observed in (Ga,Mn)As for more than 2% doping.

In the QMC results for the single-impurity case, we have observed the extended nature of the induced charge density and the spin polarization around the impurity site with a range ℓ_0 determined by model parameters such as the hybridization, the bare band structure of the host, the Coulomb repulsion, etc. In the two-impurity case, when the polarization clouds overlap, the QMC results showed that FM correlations develop between the impurities. Then, the interesting question is what happens for finite density of impurities as the average separation of the impurities becomes comparable to ℓ_0 . Does the Haldane–Anderson model capture the insulator–metal transition observed in (Ga,Mn)As? In addition, is it possible to describe the electronic properties of the metallic state bordering the insulator–metal transition as that of a disordered valence band with weak correlation effects? Or, does the metallic state retain more

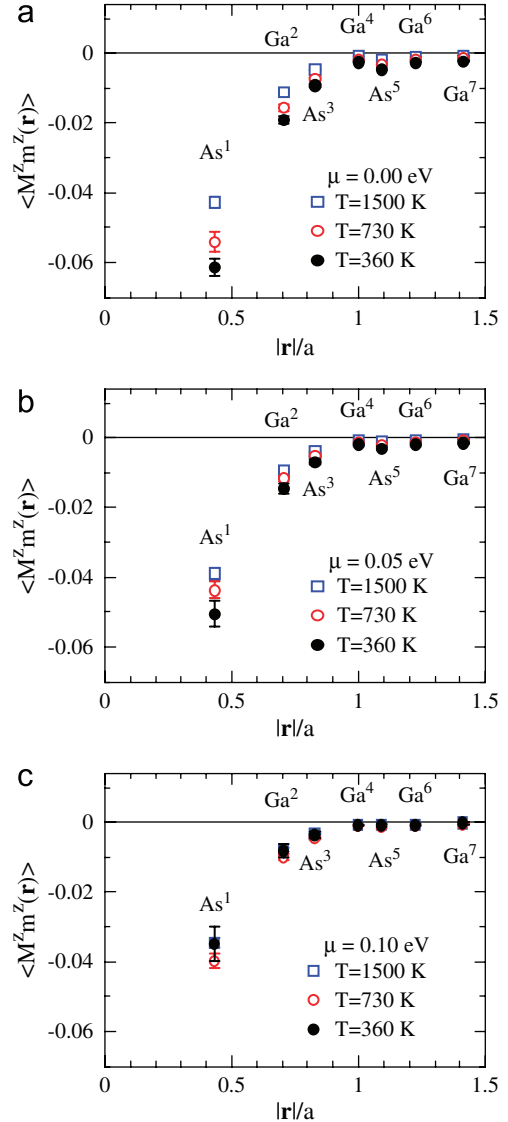


Fig. 16. (Color online) Impurity–host magnetic correlation function ($\langle M^z m^z(\mathbf{r}) \rangle$) vs. r/a at various T for (a) $\mu = 0.00$ eV, (b) 0.05 eV and (c) 0.10 eV for the single-impurity Haldane–Anderson model within the tight-binding model. Here, M^z is the magnetization operator at the Mn xy orbital.

properties of the single-impurity case so that the IBS and the split-off states continue to play roles even though they emerge with the valence band? In this case, what is the nature of the magnetic correlations among the impurities? It would be interesting to study this problem even in the simplest case where each impurity has one orbital and the density of states of the bare host and the hybridization are constants as discussed in Section 3. By extending the QMC calculations to the finite-density case, we think that it would be possible to address the question of whether the metallic state bordering the insulator–metal transition has unusual electronic properties.

7. Summary

In this paper, we studied the single- and two-impurity Haldane–Anderson models using the Hirsch–Fye QMC technique. Our purpose was to develop a microscopic understanding of the low-doping insulating phase of the DMS material (Ga,Mn)As. We first discussed the simple case where each impurity consists of

one localized orbital and the host band structure is described by 2D and 3D quadratic bands. We have presented QMC results on the inter-impurity and impurity–host magnetic correlations and the charge density around the impurity site. We observed that the presence and the occupation of the IBS is important in determining the magnetic correlations. We saw that long-range FM correlations, which are induced by the AFM coupling of the valence electrons to the impurity moment, develop between the impurities when the chemical potential is between the valence band and the IBS. We have also showed that, in the low-doping limit, the magnetic correlations between the impurities do not exhibit RKKY-type oscillations in a semiconductor. These calculations also displayed how the model parameters determine the magnetic correlations.

In order to develop a more realistic model of the low-doping insulating phase of (Ga,Mn)As, we used the tight-binding approximation to map the system to the Haldane–Anderson Hamiltonian. In this approach, we used tight-binding parameters determined from the photoemission experiments and kept all three of the Mn t_{2g} orbitals in the QMC calculations. The resulting value for ω_{IBS} is close to the experimental value of 110 meV. We also observed that the magnetic correlations weaken as the IBS becomes occupied. These results are useful for developing a microscopic understanding of the low-doping insulating phase of (Ga,Mn)As.

Acknowledgments

This work was supported by the NAREGI Nanoscience Project and a Grant-in Aid for Scientific Research from the Ministry of Education, Culture, Sports, Science and Technology of Japan, and NEDO.

References

- [1] S. Maekawa (Ed.), *Concepts in Spin Electronics*, Oxford University Press, Oxford, 2006.
- [2] H. Ohno, H. Munekata, T. Penney, S. von Molnar, L.L. Chang, *Phys. Rev. Lett.* 68 (1992) 2664;
- [3] I. Žutić, J. Fabian, S. Das Sarma, *Rev. Modern Phys.* 76 (2004) 323.
- [4] T. Jungwirth, J. Sinova, J. Masek, J. Kucera, A.H. MacDonald, *Rev. Modern Phys.* 78 (2006) 809.
- [5] R.A. Chapman, W.G. Hutchinson, *Phys. Rev. Lett.* 18 (1967) 443.
- [6] J.S. Blakemore, W.J. Brown, M.L. Stass, D.D. Woodbury, *J. Appl. Phys.* 44 (1973) 3352.
- [7] J. Okabayashi, A. Kimura, O. Rader, T. Mizokawa, A. Fujimori, T. Hayashi, M. Tanaka, *Phys. Rev. B* 64 (2001) 125304.
- [8] K.S. Burch, D.B. Shrekenhamer, E.J. Singley, J. Stephens, B.L. Sheu, R.K. Kawakami, P. Schiffer, N. Samarth, D.D. Awschalom, D.N. Basov, *Phys. Rev. Lett.* 97 (2006) 087208.
- [9] A.M. Yakunin, A.Yu. Silov, P.M. Koenraad, J.H. Wolter, W. Van Roy, J. De Boeck, J.-M. Tang, M.E. Flatte, *Phys. Rev. Lett.* 92 (2004) 216806.
- [10] D. Kitchen, A. Richardella, J.-M. Tang, M.E. Flatte, A. Yazdani, *Nature* 442 (2006) 436.
- [11] T. Jungwirth, J. Sinova, A.H. MacDonald, B.L. Gallagher, V. Novak, K.W. Edmonds, A.W. Rushforth, R.P. Campion, C.T. Foxon, L. Eaves, E. Olejnik, J. Masek, S.-R. Eric Yang, J. Wunderlich, C. Gould, L.W. Molenkamp, T. Dietl, H. Ohno, *Phys. Rev. B* 76 (2007) 125206.
- [12] F.D.M. Haldane, P.W. Anderson, *Phys. Rev. B* 13 (1976) 2553.
- [13] J.E. Hirsch, R.M. Fye, *Phys. Rev. Lett.* 56 (1986) 2521.
- [14] M. Ichimura, K. Tanikawa, S. Takahashi, G. Baskaran, S. Maekawa, in: S. Ishioka, K. Fujikawa (Eds.), *Foundations of Quantum Mechanics in the Light of New Technology (ISOM-Tokyo 2005)*, World Scientific, Singapore, 2006, pp. 183–186 (cond-mat/0701736).
- [15] K. Tanikawa, S. Takahashi, M. Ichimura, G. Baskaran, S. Maekawa, unpublished.
- [16] N. Bulut, K. Tanikawa, S. Takahashi, S. Maekawa, *Phys. Rev. B* 76 (2007) 045220.
- [17] P.M. Krstajić, V.A. Ivanov, F.M. Peeters, V. Fleurov, K. Kikoin, *Europhys. Lett.* 61 (2003) 235.
- [18] K. Yamauchi, H. Maebashi, H. Katayama-Yoshida, *J. Phys. Soc. Japan* 72 (2003) 2029.
- [19] J. Inoue, S. Nonoyama, H. Itoh, *Phys. Rev. Lett.* 85 (2000) 4610.
- [20] R.M. Fye, J.E. Hirsch, *Phys. Rev. B* 38 (1988) 433.
- [21] R.M. Fye, J.E. Hirsch, D.J. Scalapino, *Phys. Rev. B* 35 (1987) 4901.
- [22] J.E. Gubernatis, J.E. Hirsch, D.J. Scalapino, *Phys. Rev. B* 35 (1987) 8478.
- [23] J.C. Slater, G.F. Koster, *Phys. Rev.* 94 (1954) 1498.
- [24] D.J. Chadi, M.L. Cohen, *Phys. Stat. Sol. (b)* 68 (1975) 405.
- [25] B. Gu, N. Bulut, S. Maekawa, unpublished (arXiv:0804.3436).
- [26] W.A. Harrison, *Electronic Structure and the Properties of Solids*, Dover, New York, 1989.
- [27] Y. Tomoda, Master's Thesis, Tohoku University, 2008.
- [28] J. Okabayashi, A. Kimura, O. Rader, T. Mizokawa, A. Fujimori, T. Hayashi, M. Tanaka, *Phys. Rev. B* 58 (1998) R4211.
- [29] J.-M. Tang, M.E. Flatte, *Phys. Rev. Lett.* 92 (2004) 047201.